



LAWRENCE
LIVERMORE
NATIONAL
LABORATORY

Time-Resolved Microscope System to Image Material Response Following Localized Laser Energy Deposition: Exit Surface Damage in Fused Silica as a Case Example

R. N. Raman, R. A. Negres, S. G. Demos

June 16, 2010

Optical Engineering

Disclaimer

This document was prepared as an account of work sponsored by an agency of the United States government. Neither the United States government nor Lawrence Livermore National Security, LLC, nor any of their employees makes any warranty, expressed or implied, or assumes any legal liability or responsibility for the accuracy, completeness, or usefulness of any information, apparatus, product, or process disclosed, or represents that its use would not infringe privately owned rights. Reference herein to any specific commercial product, process, or service by trade name, trademark, manufacturer, or otherwise does not necessarily constitute or imply its endorsement, recommendation, or favoring by the United States government or Lawrence Livermore National Security, LLC. The views and opinions of authors expressed herein do not necessarily state or reflect those of the United States government or Lawrence Livermore National Security, LLC, and shall not be used for advertising or product endorsement purposes.

Time-resolved microscope system to image material response following localized laser energy deposition: exit surface damage in fused silica as a case example

Rajesh N. Raman, Raluca A. Negres, Stavros G. Demos

Lawrence Livermore National Laboratory, 7000 East Ave, Livermore, CA, USA
94550

This paper was presented in part at the SPIE conference on Laser Induced Damage in Optical Materials, Sept. 2009, Boulder, Colorado which appeared (unrefereed) in SPIE Proceedings Vol. 7504.

ABSTRACT

The dynamics of material response following initial localized energy deposition by the laser pulse on the material's surface is still largely unknown. In this work we describe a time-resolved microscope system that enables the study of the sequence of events and the individual processes involved during the entire timeline from the initial energy deposition to the final state of the material, typically associated with the formation of a crater on the surface. To best capture individual aspects of the damage timeline, this system can be configured to multiple imaging arrangements, such as multi-view image acquisition at a single time point, multi-image acquisition at different time points of the same event, and tailored sensitivity to various aspects of the process. As a case example, we present results obtained with this system during laser-induced damage on the exit surface of fused silica.

Subject Terms: Time-resolved imaging, microscopy, laser damage, laser ablation, fused silica

1. INTRODUCTION

1.1 Background

Coupling of laser energy into a material is associated with complex laser-matter interactions and subsequent modifications in its local structure. Such conditions are found during the ablation of materials in various applications such as laser micromachining, laser drilling and cutting, laser surgery, and pulsed laser deposition for the growth of thin films [Phipps]. With ever-increasing precision processing requirements, a better understanding of how energy is deposited and the nature of the material response would, for a specific set of laser parameters, allow one to more accurately estimate the volume of material removed and collateral mechanical damage and to tailor these processes to meet the specific application requirements. In addition, such knowledge can be utilized to devise methods to help prevent, repair, or contain undesirable effects due to laser energy deposition that ultimately lead to material failure, such as that which can occur in the case of optical components employed in high energy laser systems.

Post-mortem examination of laser-modified material using scanning and transmission electron microscopies have revealed the structural characteristics of laser-induced craters in various materials [Haglund, Craciun, Wong]. However, reconstructing the sequence of events leading to these permanent modifications requires information on the transient material response. Previous studies employed various pump-and-probe techniques, in which the material was modified by an ablating laser pulse (*pump*) and the response was captured with a *probe* pulse that was time-delayed with respect to the pump. Most of these studies have attempted to capture the dynamic processes involved using a single probe arrangement. For such a case, the interpretation of the experimental results relies on the exact reproducibility of the events and, for the estimation of the kinetics, the assumption that all observed features (such as stress fields and material clusters) originate at $t=0$, the time of the arrival of the ablating pulse. For example, shadowgraphy imaging has provided information regarding the generation and propagation of shock waves and ejection of material [Gupta, Yoo, Salleo, Zeng]. Transient changes in material phase state and structure have been studied with the aid of reflectance microscopy [Sokolowski], electron diffraction [Ihee], and x-ray diffraction [Rousse, Lindenberg], with temporal resolution ranging from several ns down to ~ 100 fs. A limited number of studies have included imaging of the same event with multiple modalities

[Rousse, Salleo] in order to take advantage of the enhanced sensitivity of each modality to a particular aspect of the ablation event. This approach provides a more complete description of the event and allows one to better correlate separate observations (such as changes in material reflectance with shock wave generation) occurring simultaneously. Only a small number of studies have probed the same event at multiple time points in order to more accurately capture the kinetics of the dynamic material response [Jiang, Lindenberg]. These previous studies have shown the feasibility of dynamically imaging these events and have provided the groundwork for the design of a more advanced, versatile dynamic imaging system which in principle could provide more comprehensive information on the various aspects of an ablation event. Furthermore, it is important to investigate the material response at longer delays ($> \sim 100$ ns) following the pump pulse as the cooling phase can be on the order of 100s of μ s or longer.

In this work we describe a time-resolved microscope system designed to enable imaging of the sequence of events and the individual processes involved during the entire timeline from the initial energy deposition to the final state of the material with adequate sensitivity and spatial and temporal resolution. This system is configurable into multiple imaging arrangements, such as multi-view image acquisition at a single time point, multi-image acquisition at different time points of the same event, and tailored sensitivity to various aspects of the process. The system is designed to provide detailed information on the processes involved and material response, including a) kinetics of shock wave propagation, b) the time of particle (material cluster) ejection and their instantaneous speed and 3-dimensional motion, and c) transient material phases and behaviors.

To demonstrate the capabilities of the time-resolved imaging system presented in this work, we show images capturing the response of fused silica samples with flat polished surfaces following laser energy deposition on their exit surface, commonly referred to as exit surface laser-induced damage. This process is typically associated with material ejection and the formation of a crater on the surface. We chose this example for two main reasons: 1) only a small portion of the surface that is exposed to the laser beam initiates localized energy deposition (damage) and thus, we can better understand the interaction of the modified material (and plasma) with the laser pulse, and 2) the plasma forming at the material interface is illuminated from the bulk side, which allows the investigation of the interaction of the material with the laser pulse without interference from shielding effects (by the plasma expanding on the air side).

1.2 System Requirements

In order to successfully capture all of the important aspects during the entire timeline of a laser ablation or damage event, the system must provide adequate sensitivity to detect the various dynamic components of material response involved and produce images with appropriate spatial and temporal resolution to estimate the material kinetics leading to crater formation, the onset and propagation of shock fronts, and the nucleation of material transformations and transport. In addition, this system needs to accurately estimate ejected material size, speed, trajectory, and time of ejection (relative to the arrival of the damage pulse). Furthermore, the static spatial resolution needs to be maintained when imaging dynamic phenomena ($\sim 1 \mu\text{m}$)

2. EXPERIMENTAL SYSTEM AND PRELIMINARY RESULTS

2.1 Sample preparation and laser energy deposition protocol

Experiments were conducted on circular fused silica optical flats 5 cm in diameter and 1 cm in thickness. A 15-cm focal length lens was used to focus the output of a laser (Quanta-Ray, Spectra-Physics) operating at 355 nm (3ω), 7.5-ns full-width at half maximum (FWHM) in duration, about 2 cm behind the exit-surface of the sample. In this arrangement, we estimate the pump beam diameter at the exit surface to be ~ 1 mm with nearly flat top spatial profile. Pristine surface locations were exposed to a single laser pulse with average fluence of $\sim 30 \text{ J/cm}^2$ leading to damage initiation with 80% probability. This procedure led to the formation of single or multiple pit craters on the order of 10-50 μm in diameter on average.

2.2 Basic time-resolved microscope system design for imaging crater formation and material ejection

Shadowgraphy has proven to be a useful tool for imaging the material motion following laser ablation in various material systems [Gupta, Yoo, Salleo, Jiang, Zeng]. Since laser-induced surface damage is also associated with material ejection and the formation of craters during a laser damage event, the basic system was designed to be able to capture these main processes. In particular, the simultaneous recording of images that capture both the material ejection process and the formation of the damage site (namely the evolution of its lateral dimensions) was needed. To achieve this capability, two microscope systems were employed with the focal plane of the first microscope

positioned parallel to, while that of the second microscope was positioned perpendicular to, the surface of the sample optic. The focal planes of the two microscopes intersected at the sample's surface at the pump beam location. Both microscopes were identical, utilizing a long working distance 5X objective (Mitutoyo) followed by a 5X zoom lens. The images were focused onto separate charge-coupled devices (CCD, Spiricon, 1616 pixels \times 1216 pixels) with individual pixel size of 4.4 μm , resulting in a 755 μm \times 569 μm field of view. The corresponding images are referred to as the transmission-view (TV) and side-view (SV) images, respectively. A schematic of this system is provided in Fig. 1(a). The static spatial resolution was on the order of 1 μm , as measured by imaging a standard resolution target (Fig. 1(b)).

The images were captured using strobe-light illumination provided by a 532 nm wavelength (2ω) probe pulse (Litron Lasers) about 4.5 ns in duration (FWHM). The timing of the probe pulse output was controlled by an adjustable delay trigger in reference to the pump pulse, allowing for the imaging of various time points during the entire timeline of damage initiation and growth events. While the pump-probe pulse jitter was ~ 2 ns, for each event we recorded the relative time delay between pump and probe with ~ 0.5 ns resolution.

To remove static features in the image arising from non-uniformities in the probe laser beam spatial profile, all images were divided pixel-by-pixel by a reference image of the pristine site (prior to damage). Figure 2 shows examples of removal of such artifacts via image processing. In particular, Figs. 2(a-b) illustrate (a) a raw transient image at 0 ns delay and (b) the same image after normalization in the SV mode. As a result, the interference fringes caused by partial reflection of the probe beam on the sample surface are largely removed. Similarly, in Figs. 2(c-d), background non-uniformities in a static transmission image are likewise removed.

Representative images obtained with the basic system are shown in Fig 3. Figures 3(a-c) display images captured by the SV microscope (damage sites at three different locations). Figure 3(a) shows a SV image at 25 ns delay after exposure to the damage pulse. Several shock fronts are visible which appear to originate from different points on the surface and travel through the air. However, no material motion is seen in this early delay time image. Figure 3(b) displays a SV image taken at 400 ns delay. A jet of particles is visible originating from the surface and traveling through the air.

Particles near the surface are close together and in focus while those further downstream are more spread out and, as a result, during image acquisition at longer delays some are outside the in-focus imaging zone of the microscope system (with depth of focus on the order of 40 μm). The diameters of the observed particles are on the order of 1-10 μm . Also visible is the shock front traveling through the air with several particles ahead (downstream) of this front.

For estimating ejecta kinetics from the SV images, it is necessary to precisely locate the surface of the sample, i.e. the origin of ejected particles. To identify the location of the surface, images of the damaged surface were acquired by the SV microscope after blocking the SV beam path, thus imaging the photons from the TV beam path that were scattered at the damage site. An example of a scattering image after several scattering sites (corresponding to several damage sites) had been formed is shown in Fig. 3(c). These sites are visible as a series of vertically-oriented bright spots on the right hand side. In this manner, the location of the sample exit surface in the SV images can be determined.

Figures 3(d-e) display TV images of the same damage site captured at two different points in time. Specifically, Fig. 3(d) displays a transient transmission image of a damage initiation site at 7 ns delay, while Fig. 3(e) displays the final crater several seconds later. These images show a difference in lateral dimensions of the crater, revealing that the crater is evolving over this time scale. Separate initiation sites appear to form but grow to the point where some of them coalesce.

2.3 Backscattering illumination configuration for increased sensitivity to early material motion

The results shown in Fig. 3(a) indicate that material changes occurring at earlier times are only partially visualized due to the obscuration in the SV beam caused by the shock front in the air. Thus, for detecting early material motion, a different configuration is required.

In general, dark-field microscopy is better able to detect small isolated particles than bright-field. For this reason, we modified the previous configuration by removing the beam-splitter and rearranging the mirrors so as to illuminate the sample from the same direction as the image formation; the probe beam was directed onto the exit surface from behind the sample (incident at ~ 60 degrees with respect to the sample's exit surface normal), as shown in Fig. 4. In this arrangement, transient images of damage site formation were recorded by the TV CCD (#1) and SV CCD (#2). Thus, material motion or ejection becomes visible from light directly scattered from the

material (dark-field) rather than as a result of material obscuration (bright-field). All other laser damage and imaging parameters remained the same as in the basic system shown in Fig. 1.

Figure 5 compares images acquired in the SV shadowgraphy (bright-field) mode described in section 2.1.1 to those acquired using backscattering (dark-field) mode at the same delay times. These images are all from different but similar damage events. Figures 5(a-b) show images acquired at 300 ns delay, both of which capture the particle ejection process. The additional benefit offered by backscattering is apparent when viewing images at early delay times. As an example, at 25 ns delay time only the shock front is visible in the shadowgraphy mode (Fig. 5(c)), whereas material motion located behind the shock front is observable in the backscattering configuration (Fig. 5(d)). The images suggest that a swelling of the surface precedes the ejection of individual particles, capturing a critical part of the early material response to localized energy deposition that would otherwise not be observable in the shadowgraphy mode.

2.4 Dual-probe configuration for measuring the ejected particles' kinetic properties

More accurate information regarding shock wave and particle trajectory and motion can be obtained by visualizing the same event at multiple time points. While the two previous system configurations are able to capture material motion and shock propagation spanning the entire timeline of an exit-surface damage event, they can only capture one transient image per distinct event. However, the total amount of energy deposition may be different at various sites due to surface non-uniformities and shot-to-shot variation in the pump pulse energy. This practical consideration necessitated an additional experimental configuration that could more accurately estimate the kinetic properties of material clusters and the propagation characteristics of shock fronts from individual events. Our approach is to employ dual image acquisition per event in order to better quantify the relative motion of various objects and disturbances in the image.

To capture images at two different delay times within the same event, a second 532 nm probe laser was added to the basic system whose pulse was delayed with respect to that of the first probe (Fig. 6). To differentiate the images from each probe, we utilized a polarization filtering method in which the output polarizations of the two probe beams were set orthogonal to each other. The two beams were then combined using a polarizing beam-splitter into a single beam path. Next, a standard (non-polarizing) beam-splitter was used to establish a TV path (transmitted beam) and a SV path

(reflected beam), illuminating the sample in the same geometry as in the basic system (Fig. 1). The two illumination pulses from the SV path (delayed with respect to each other) were then imaged using the same microscope system previously described. A final polarizing beam-splitter positioned after the microscope's image-forming optics separated the two orthogonal polarization image components and directed them to separate CCDs. The time delays between the two probe pulses ranged from 100 to 500 ns.

For calibration and image co-registration between the two SV cameras, probe 2 was turned off and a quarter-waveplate was inserted into the probe 1 path in order to illuminate the sample with circular polarization. This polarization state permitted simultaneous imaging of the same event in both SV cameras. Subsequently, the location of the sample's surface was determined on each camera as well as the shift in pixel coordinates between the two cameras when imaging the same object.

Following this image registration process, we were able to quantify the difference in the distance traveled from the surface by individual particles or shock fronts between the two delay times. This information allows us to more accurately estimate the instantaneous velocity of a particle or shock front. As a typical example, Fig. 7(a) shows particle ejecta at 2 μs delay, while Fig. 7(b) shows an image of the same event 500 ns later (at 2.5 μs delay) when the particles have traveled further from the surface. The relative positions of the particles do not change for the most part, allowing for co-registration of most particles. In addition to translational motion, many particles can be seen to exhibit rotational motion. For instance, the particles denoted as 1-6 in Fig. 7 exhibit different projected dimensions at the two time points, providing information on their 3-dimensional shape.

2.5 Configuration for imaging high-velocity phenomena with optimal spatial resolution

A limitation in temporal resolution existed for the imaging of the shock front in air and in the material, the early motion of the surface, and fast ejected particles due to high speeds across the field of view. For instance, the speed of the pressure front generated following laser energy deposition in fused silica is on the order of the speed of sound in the material, $\sim 6 \mu\text{m/ns}$. In this case, the ~ 4.5 ns probe pulse could only provide spatial resolution on the order of 30 μm when capturing these events. To resolve the dynamics of these key parameters exhibiting high speed within the $\sim 1 \mu\text{m}$ spatial resolution of the imaging system, the pulse length of the laser should be sufficiently short. For example, to resolve the pressure front with 1 μm spatial resolution, the probe pulse length should be

about 170 ps. Furthermore, the imaging system must be able to capture two images per each event spaced closely in time (sub-nanosecond) in order to better estimate instantaneous speed as this may be changing during the timeline.

To meet these requirements, the probe lasers 4.5 ns in pulse duration described in section 2.2 were replaced with a laser with a pulse length of ~ 150 ps (EKSPLA, Lithuania). To allow for dual imaging per event, two probe pulses (probe 1 and probe 2) were generated by splitting the output from the 150 ps laser into two paths using a non-polarizing beam-splitter. The reflected beam (probe 2) was directed towards an adjustable delay line of length of ~ 60 cm roundtrip, providing an adjustable delay of up to ~ 4.15 ns with respect to the transmitted beam (probe 1). A half-wave plate was inserted within the delay line in order to rotate the polarization of probe 2 to a state orthogonal to that of probe 1 (to allow for polarization filtering as described in section 2.4.1). Both probe beams were then combined using a polarizing beam-splitter. The combined beam was subsequently split into a SV path and a TV path as described in section 2.4.1 and illuminated the sample. A polarizing beam-splitter positioned after the TV image formation optics separated the two orthogonal polarization image components (delayed with respect to each other) which were recorded on separate cameras (Fig. 8(a), CCDs 1-2). The temporal profiles of the pump and probe pulses were recorded using a high-speed GaAs photodetector (rise time < 35 ps, Electro-Optics Technology, Inc.) and digital oscilloscope (Tektronix) with sampling rate capability of 25 Gsamples/s.

Typical higher temporal resolution images acquired in the TV mode are shown in Fig. 9. These images reveal the material response during energy deposition by the pump pulse (Figs. 9(a-b)) with the timing of the probe pulses illustrated in Fig. 9(d). In particular, the probe 1 pulse arrived ~ 0.7 ns before the peak of the pump pulse (defined as delay $\tau = 0$), while the probe 2 pulse arrived at $\tau \sim 0.5$ ns delay. From these images, one sees that the material begins to optically absorb early on during the damage initiation process and these absorbing regions grow in size during exposure to the laser pulse. The final dimensions of the damage craters are much larger as can be seen in Fig. 9(c).

This system can also be used to measure the transient stress fields generated by the propagating pressure wave. This is achieved by blocking the probe 2 path in Fig. 8(a) and utilize only probe 1. The polarizing beam-splitter following the TV imaging optics can be used to separate and capture the image component with polarization state parallel to that of the probe 1 beam and the image

component with perpendicular polarization state. The former component is conventional shadowgraphy, while the latter provides a map of the locations in the material where a rotation of the polarization state of the probe beam is induced, such as by local stress fields.

Figure 10 shows examples of transient parallel and orthogonal polarization TV images taken at $\tau \sim 13.4$ ns delay. The parallel polarization image (Fig. 10(a)) represents the conventional shadowgraphy image showing the region of the material that has been modified and the shock in the air side of the interface. Locations of increased intensity are observed in the orthogonal polarization image arising from the presence of stress in the material (bright features in Fig. 10(b)) due to the propagation of the shock front(s). In the final images (not shown), residual stress in the material was only observed near where cracks had been formed. This configuration is particularly useful for estimating the kinetics of the shock waves in both the air and in the bulk of the material at the surface.

It must be noted that the system shown in Fig. 8 can also be used to image with high temporal resolution the expansion of the damage site and the propagating stress fields inside the bulk of the material using the SV mode while acquiring the images through the bulk of the material. This can be achieved when the material is transparent or semi-transparent and the side of the sample is polished to allow high quality image acquisition. In addition, high-resolution imaging of shock fronts propagating in the air and material motion at early delay times, such as those illustrated in Figs.5(c-d), can be performed.

3. DISCUSSION

Material response to laser energy deposition is multi-faceted, consisting of the generation of extreme temperatures and pressures over a microscopic volume leading to transient material phase transformations, the generation and propagation of stress fields (shock fronts), material motion and ejection, and crater formation. The task of describing this entire timeline is not suited for a single measurement modality. In this work we presented a time-resolved microscopy system with adaptable configurations where each is optimized for a particular aspect of the material response to laser energy deposition. We demonstrate the capabilities of this system by examining the specific case of laser-induced damage on the exit surface of fused silica polished flats.

The basic system configuration of Fig. 1 provides simultaneous SV and TV shadowgraphic imaging of the same event and has been demonstrated before as separate systems (not as a combined system) [Gupta, Yoo, Salleo, Zeng]. SV illumination permits the probing of a number of features, namely the kinetics of material cluster ejection and stress field propagation. Material clusters appear as dark features because they are obscuring the probe beam illumination via absorption and/or scattering. The shock front on the air side is visible because of the modulation it creates in the refractive index in air. With this system, average speeds of the particles and shock fronts can be estimated from the delay time of the probe pulse and distance traveled, assuming that the process started upon the arrival of the damage pulse ($\tau = 0$ s).

TV images provide views of the lateral expansion of the modified material volume and subsequently the formation of the crater. As the absorption and scattering properties of the host material change in response to laser energy deposition, the modified material volume appears as a dark object. Transmission loss dynamics can be measured when comparing an image in the transient state (during which the material is still undergoing modifications due to changing local temperatures and pressures) to that in the initial and/or final state (the latter represents the classical damage pit observed following a damage event). For example, the absorbing regions in Figs. 3(b-c) are observed to continue to grow laterally for about 25 ns. Information obtained via simultaneous TV and SV imaging makes possible the correlation between changes in lateral dimensions with shock wave generation, material swelling, and particle ejection. For accurately capturing the dynamics involved at early delay times, it is critical to determine the location of the surface and employ the highest possible spatial resolution.

Although shadowgraphic imaging can provide a wealth of information, the backscattering imaging configuration depicted in Fig. 4 provides better sensitivity in detecting early material motion near the surface. This configuration is inherently sensitive to detecting small isolated particles and permits usage of the detector's full dynamic range. Similar to the SV configuration, the backscattering configuration shows a jet of ejected material clusters. While not able to detect the shock front in the backscattering mode, this mode has the advantage that it is sensitive to early material response behind the expanding shock front. On the other hand, artifacts like laser speckle can influence the quality of backscattering images which are largely absent in shadowgraphy.

Backscattering should also be able to detect concentrations of particles smaller than the resolution limit of the system (nano-particles) which will appear as light scattering “clouds.”

While only the average dynamic properties of ejected particles are inferable based on single-probe shadowgraphic imaging, the dual-probe configuration directly measures the average speed of the ejected particles during the time interval between the arrival of probe 1 and probe 2. This method also provides evidence that particles may have accelerated (for example when crossing the shock front) or decelerated along their trajectory from the surface. Since the projection of certain particles in the image plane (Fig. 7) changes when viewed on the probe 1 image vs. the delayed probe 2 image, these ejecta must be non-spherical (flake-like in some instances) in shape. In addition, comparison of the two images from this dual-probe setup yields information on rotational motion of the ejected particles. A very important and novel feature of this system is that it allowed us to estimate the ejection time of the particles observed in the images captured at different delay times. Preliminary results indicate that the particle ejection time can be as late as 20 μs after the arrival of the pump pulse.

With the incorporation of a probe laser source producing shorter pulses ~ 150 ps FWHM, the dynamics of material motion and disturbances can be better resolved. For example, events occurring early on during energy deposition (such as modification of the absorption properties of the exposed site) were probed at multiple time points in the TV mode. In addition, fast dynamic events occurring near the speed of sound were observable with the polarization-sensitive imaging configuration. In particular, the generation and propagation of shock waves both in air (observed in the parallel polarization image component) and within the material (observed in the orthogonal polarization image component) were observable in the transient images. In addition, polarization-sensitive imaging allowed visualization of residual stress fields in the material in the final images long after energy deposition.

In the case example of laser-induced damage on the exit surface of fused silica used in this work, the preliminary findings regarding rear surface damage in fused silica optical components caused by 7-ns FWHM, 355 nm laser pulses can be summarized by the following observations. During the early part of the laser pulse, we observed the host material to locally become more optically absorptive. Then, these absorbing regions grow in size during laser energy deposition. Next the formation of

cracks is observed, followed by growth in crack size. The material reaches a critical energy density and the explosive process begins; during the later part of the pulse, the surface of the material begins to swell. After the end of the pulse, the absorbing region continues to expand as swelling continues, and a bulge can be observed forming on the surface. After this bulge reaches its maximum size, small material clusters are observed to separate from the bulge; initially small particles at speeds up to ~ 3 km/s are ejected and form a jet, joined later by larger, slower particles. Irregularly shaped particles (resembling flakes and chips) traveling at speeds of the order of ~ 10 m/s are observed at delays on the order of several μ s, indicating that the ejection process is long-lived.

ACKNOWLEDGEMENTS

This work was performed under the auspices of the U.S. Department of Energy by Lawrence Livermore National Laboratory under Contract DE-AC52-07NA27344.

REFERENCES

- [1] C. Phipps, ed., *Laser ablation and its applications*, Springer, Boston (2007).
- [2] R. F. Haglund and D. R. Ermer, "Explosive vaporization in fused silica initiated by a tunable infrared laser," *Appl Surf Sci* **168**, 258-262 (2000).
- [3] V. Craciun, N. Bassim, R. K. Singh, D. Craciun, J. Hermann, and C. Boulmer-Leborgne, "Laser-induced explosive boiling during nanosecond laser ablation of silicon," *Appl Surf Sci* **186**, 288-292 (2002).
- [4] J. Wong, J. L. Ferreira, E. F. Lindsey, D. L. Haupt, I. D. Hutcheon, and J. H. Kinney, "Morphology and microstructure in fused silica induced by high fluence ultraviolet 3ω (355 nm) laser pulses," *J Non-Cryst Solids* **352**, 255-272 (2006).
- [5] A. Gupta, B. Braren, K. G. Casey, B. W. Hussey, and R. Kelly, "Direct imaging of the fragments produced during excimer laser ablation of $\text{YBa}_2\text{Cu}_3\text{O}_{7-\delta}$," *Appl Phys Lett* **59**, 1302-1304 (1991).
- [6] J. H. Yoo, S. H. Jeong, X. L. Mao, R. Greif, and R. E. Russo, "Evidence for phase-explosion and generation of large particles during high power nanosecond laser ablation of silicon," *Appl Phys Lett* **76**, 783-785 (2000).

- [7] A. Salleo, F. Y. Genin, M. D. Feit, A. M. Rubenchik, T. Sands, S. S. Mao, and R. E. Russo, "Energy deposition at front and rear surfaces during picosecond laser interaction with fused silica," *Appl Phys Lett* **78**, 2840-2842 (2001).
- [8] H. Jiang, J. McNary, H. W. K. Tom, M. Yan, H. B. Radousky, and S. G. Demos, "Nanosecond time-resolved multiprobe imaging of laser damage in transparent solids," *Appl Phys Lett* **81**, 3149-3151 (2002).
- [9] X. Zeng, X. Mao, S. Wen, R. Greif, and R. E. Russo, "Energy deposition and shock wave propagation during pulsed laser ablation in fused silica cavities," *J Phys D Appl Phys* **37**, 1132-1136 (2004).
- [10] K. Sokolowski-Tinten, J. Bialkowski, A. Cavalleri, and D. von der Linde, "," *Phys Rev Lett* **81**, 224-227 (1998).
- [11] H. Ihee, V. A. Lobastov, U. M. Gomez, B. M. Goodson, R. Srinivasan, C. Ruan, and A. H. Zewail, "," *Science* **291**, 458-462 (2001).
- [12] A. Rousse, C. Rischel, S. Fourmaux, I. Uschmann, et al., "Non-thermal melting in semiconductors measured at femtosecond resolution," *Nature* **410**, 65-68 (2001).
- [13] A. M. Lindenberg, J. Larsson, K. Sokolowski-Tinten, K. J. Gaffney, et al., "Atomic-scale visualization of inertial dynamics," *Science* **308**, 392-395 (2005).
- [14] R. A. Negres, M. D. Feit, S. G. Demos, "Dynamics of material modifications following laser-breakdown in bulk fused silica," *Optics Express*, *submitted*.

List of Figure Captions:

Figure 1. (a) Basic time-resolved microscope system for simultaneous acquisition of transmission-view (TV) and side-view (SV) images of surface damage sites at various points during the timeline. (b) Image of resolution slide with positive test pattern in the TV mode.

Figure 2. Image normalization using pixel-by-pixel division by a reference image of a pristine site. Full size ($755\ \mu\text{m} \times 569\ \mu\text{m}$ field of view) SV image (a) before and (b) after normalization. Zoom-in ($115\ \mu\text{m} \times 82\ \mu\text{m}$) TV image (c) before and (d) after normalization.

Figure 3. Typical images using simultaneous SV and TV imaging configuration. Full size SV images (a) at 25 ns delay, (b) at 400 ns delay, and (c) post-damage scattering image (see text for details) were obtained at three different locations. Zoom-in ($67\ \mu\text{m} \times 50\ \mu\text{m}$) of TV images illustrate (d) the transient (7 ns delay) and (e) final states of the same damage site.

Figure 4. Pump- single probe backscattering imaging configuration.

Figure 5. Comparison between SV (a) shadowgraphy and (b) backscattering modes at pump-probe delay of 300 ns. (c-d) Similarly for early delay of 25 ns. Images are from different but similar events. The size of each imaged area is $755\ \mu\text{m} \times 569\ \mu\text{m}$.

Figure 6. Pump- dual probe imaging configuration for SV multi-image acquisition of the same damage event at different pump-probe delay times.

Figure 7. (a) Side-view image ($92\ \mu\text{m} \times 103\ \mu\text{m}$) at pump-probe delay of 2 μs . (b) Image of same event 500 ns later. Six particles are identified for comparison.

Figure 8. (a) Schematic of high temporal resolution, dual probe pulse, experimental arrangement.

Figure 9. Typical high temporal resolution TV images of the same damage initiation using the dual probe pulse configuration. Images captured shortly (a) before and (b) after arrival of the peak of the pump pulse. The image showing the final state of the damage site is included in (c) for reference. Each image size is $163\ \mu\text{m} \times 181\ \mu\text{m}$. (d) Plot of temporal profiles and relative arrival times of the pump, probe 1, and probe 2 pulses for this case. Arrival of the peak of the pump pulse is defined as time delay $\tau = 0$.

Figure 10. Example of high temporal resolution, polarization-sensitive images taken simultaneously in the TV mode 13.4 ns delay after the peak of the pump pulse. (a) PP = parallel polarization image component and (b) OP = orthogonal polarization image component, relative to that of the incident probe pulse. Each image size is $290\text{ }\mu\text{m} \times 305\text{ }\mu\text{m}$.

Figure 1:

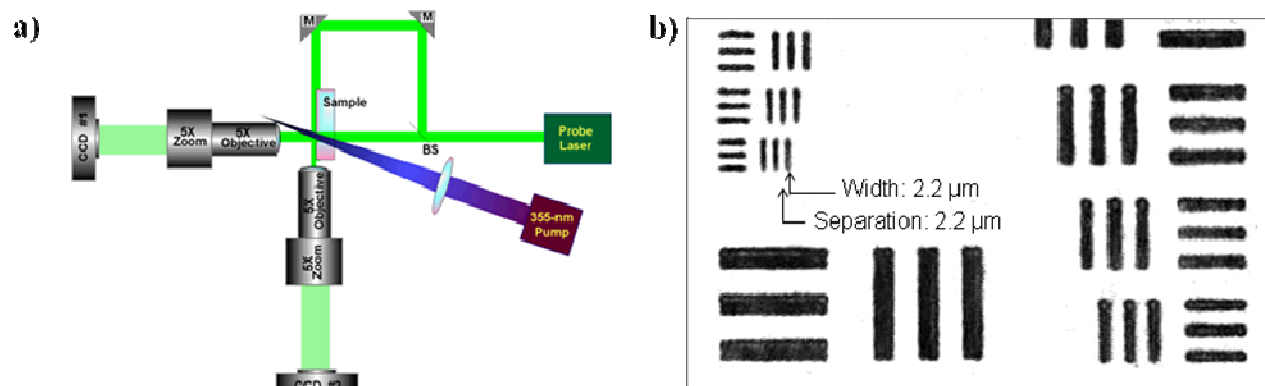


Figure 2:

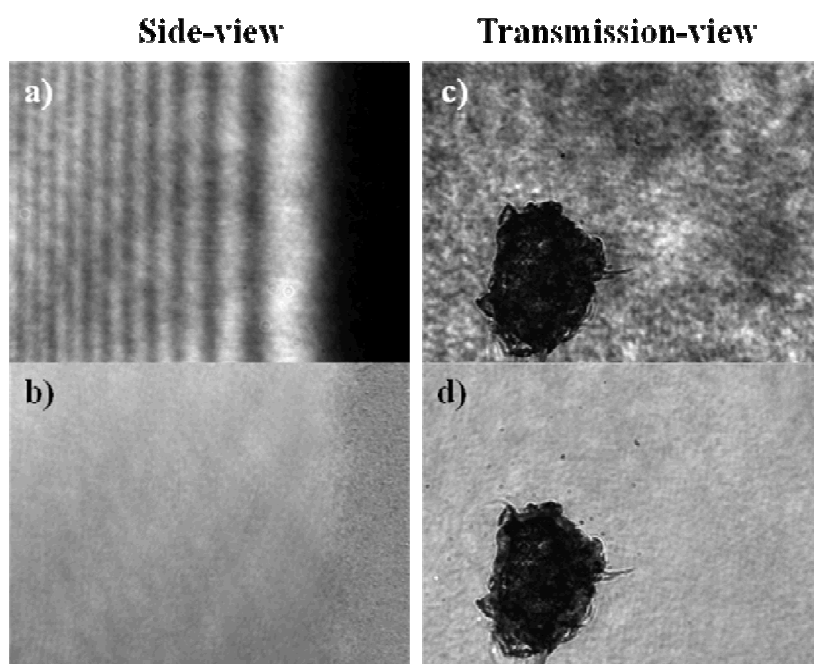


Figure 3:

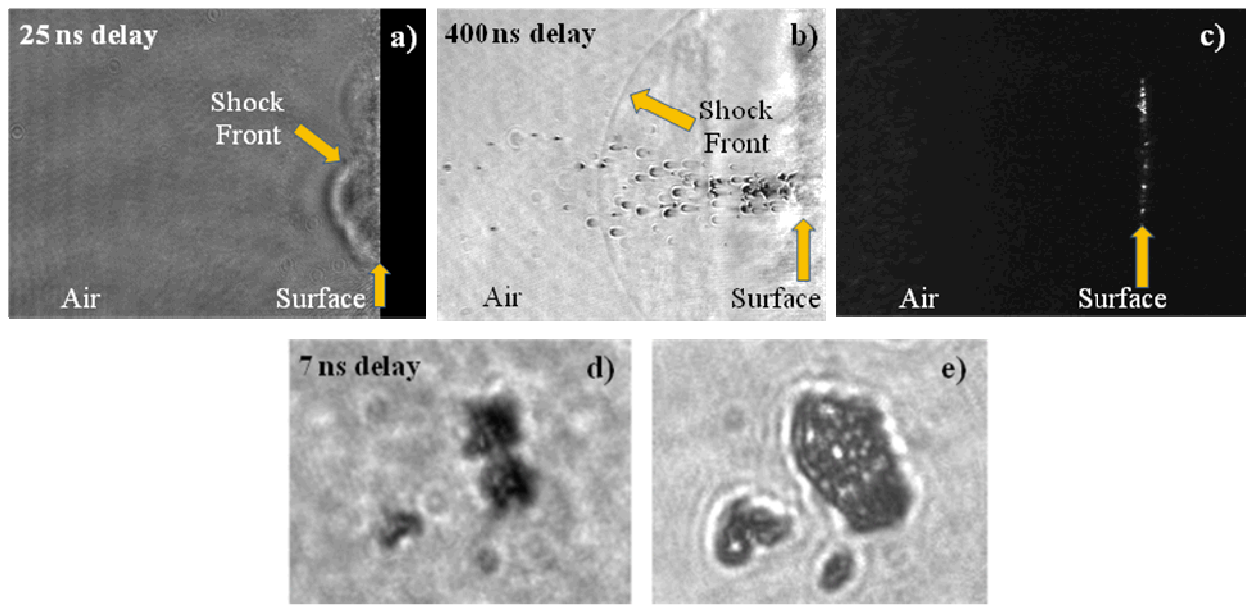


Figure 4:

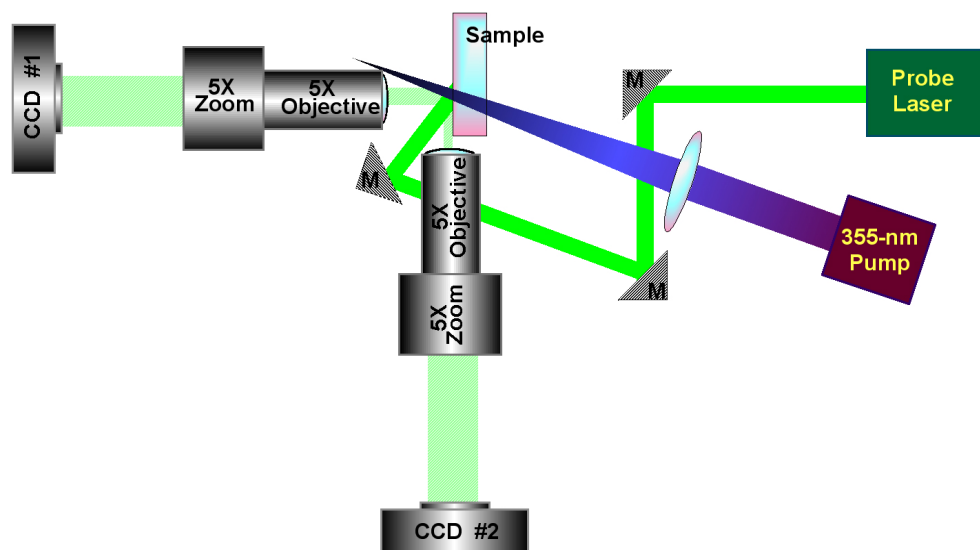


Figure 5:

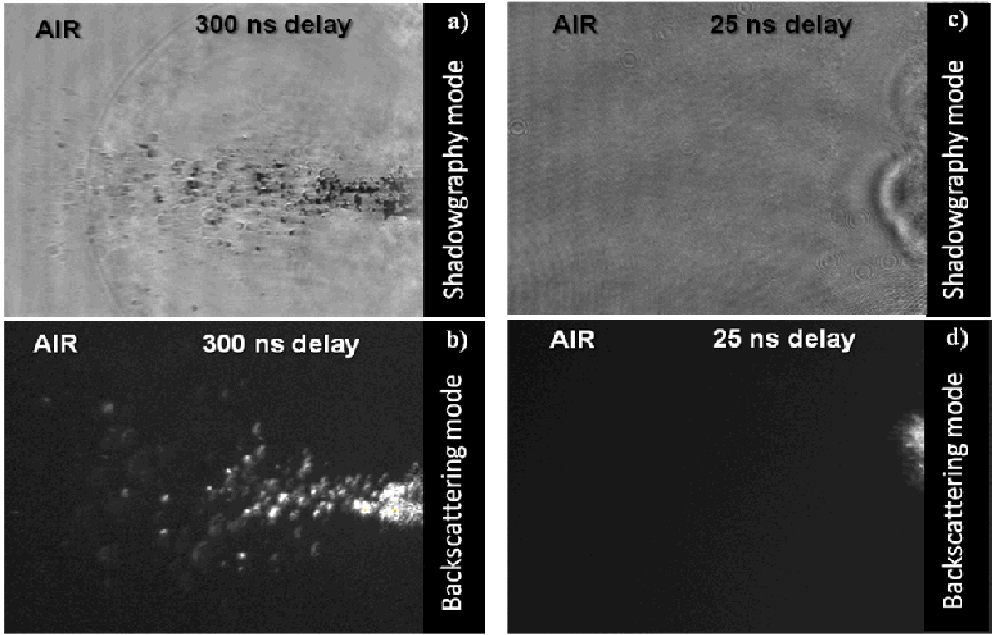


Figure 6:

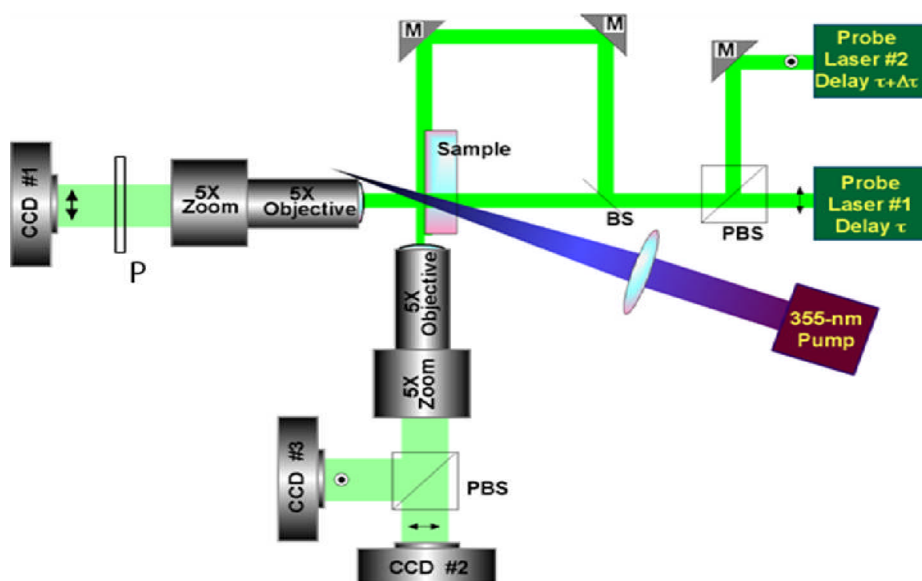


Figure 7:

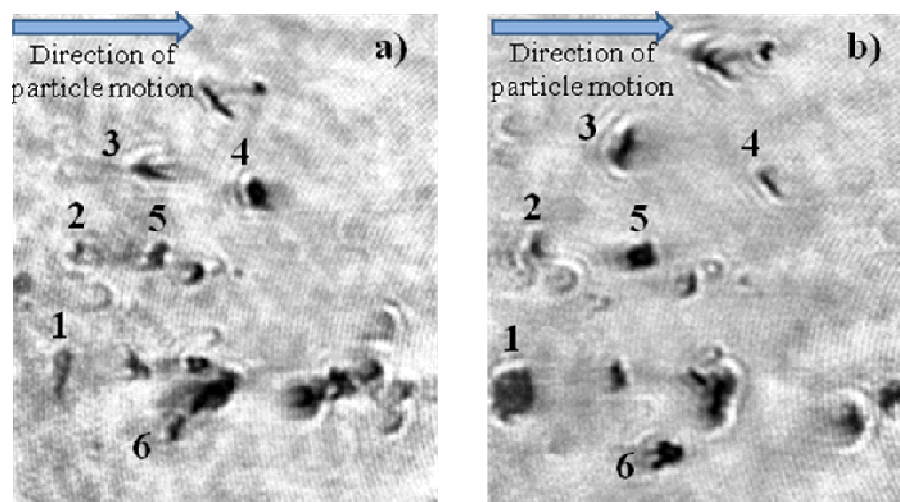


Figure 8:

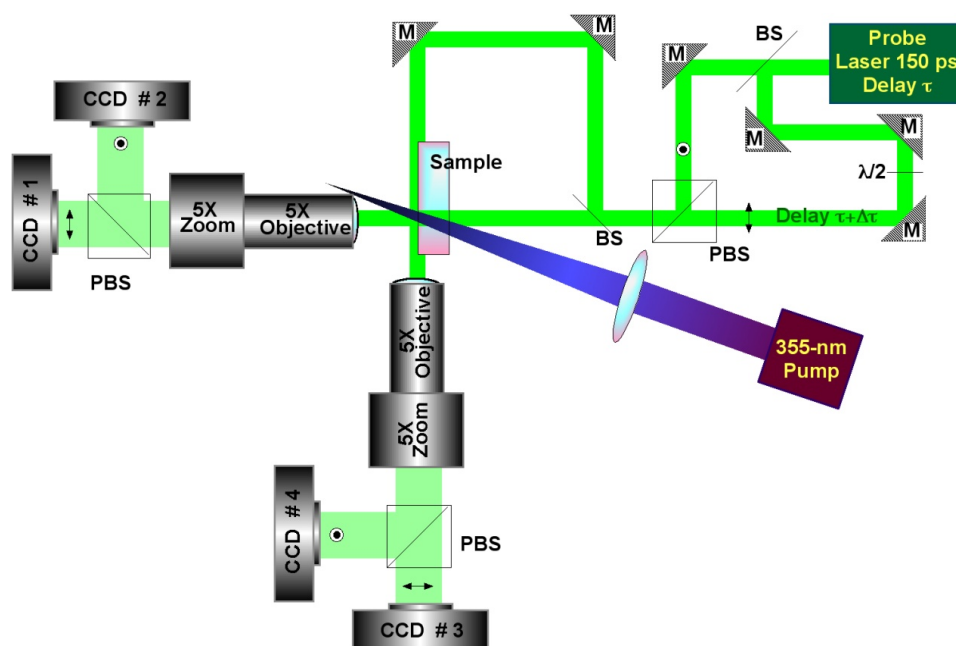


Figure 9:

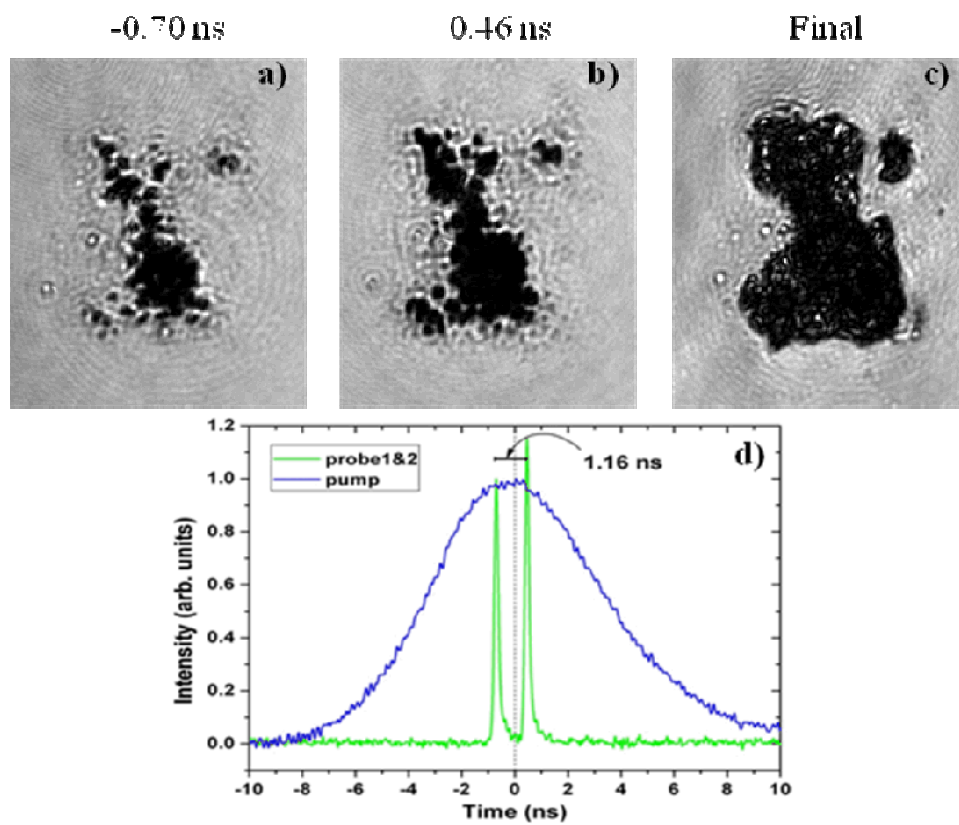


Figure 10:

